Article

Not peer-reviewed version

# Crystal Structure and Optical Second Harmonic Generation of Self-Assembled Boc-P-Nitro-L-Phenylalanyl-P-Nitro-L-Phenylalanine Dipeptide

Rosa M. F. Baptista *, Alejandro P. Ayala , Etelvina de Matos Gomes , Maria Cidália Rodrigues Castro , Ana V. Machado , Michael S. Belsley *

Posted Date: 19 November 2024

doi: 10.20944/preprints202411.1376.v1

Keywords: dipeptides; self-assembling; biomaterials; single crystal X-Ray diffraction; optical second harmonic generation

*Article*

# Crystal Structure and Optical Second Harmonic Generation of Self-Assembled Boc-*p*-nitro-L-phenylalanyl-*p*-nitro-L-phenylalanine Dipeptide

**Rosa M. F. Baptista [1,*], Alejandro P. Ayala [2], Etelvina de Matos Gomes [1], M. Cidália R. Castro [3], Ana V. Machado [3] and Michael S. Belsley [1,*]**

[1] Centre of Physics of Minho and Porto Universities (CF-UM-UP), Laboratory for materials and Emergent Technologies (LAPMET), University of Minho, Campus de Gualtar, 4710-057 Braga, Portugal
[2] Departamento de Física, Universidade Federal do Ceará, Fortaleza, CE 65455-900, Brazil
[3] Institute for Polymers and Composites, University of Minho, Campus de Azurém, 4800-058 Guimarães, Portugal
* Correspondence: rosa_batista@fisica.uminho.pt ; belsley@fisica.uminho.pt

**Abstract:** Boc(Boc= tert-butoxycarbonyl)-*p*-nitro-L-phenylalanyl-*p*-nitro-L-phenylalanine, a dipeptide characterized by acentric symmetry, self-assembles into micro-tapes. This study explores its thermal, structural, and nonlinear optical properties. Thermo-gravimetric analysis reveals an onset degradation temperature of 190 ºC, with primary and secondary peaks at 202 ºC and 220 ºC, respectively. The crystal structure of the dipeptide was determined through single crystal X-ray diffraction at 100 K, confirming its crystallization in space group P2 with two molecules per unit cell. Additionally, optical second harmonic generation polarimetry indicates a significant nonlinear optical response, with an effective coefficient ($d_{eff}$) estimated to be at least 0.52 pm/V. This value is only four times lower than that of state-of-the-art phase-matched β-barium borate nonlinear crystals, highlighting the potential of this dipeptide in nonlinear optical applications.

**Keywords:** dipeptides; self-assembling; biomaterials; single crystal X-Ray diffraction; optical second harmonic generation

## 1. Introduction

Novel organic materials obtained from molecular self-assembling through low energy interactions, such as Van der Waals bonds, electrostatic interactions, hydrogen bonds and stacking interactions originate well-ordered supramolecular structures. A versatile method for creating architectures of nanostructured materials, by using amino acids as natural building blocks, is offered by self-assembled peptide-based systems, which are attracting increasing attention due to their biocompatibility and diverse structural and functional properties for applications in a variety of fields from regenerative medicine to fluorescent probes, light energy harvesting and optical waveguiding [1–4]. Due to their spontaneous process of self-organization peptide nanostructures have a great advantage of other organic materials.

Aromatic and aliphatic dipeptide nanotubes (NT) are a unique class of bio-inspired nanostructures forming simple and modifiable organic materials, which crystallize into tubular structures hundreds of nanometers long and internal diameters of tens of angstroms. These structures result from stacking of molecules through the formation of intermolecular hydrogen bonds between functional groups in the peptide backbone [5,6].

The most studied self-assembled system is L-phenylalanyl-L-phenylalanine or diphenylalanine (hereafter PhePhe) [7] which is formed by the self-assembling of the aromatic dipeptide into NT, with ere large hydrophilic channels formation as revealed by Gorbitz [8], such as nanowires [9] and

 doi:10.20944/preprints202411.1376.v1



nanorods [10] depending on the experimental conditions such as pH and temperature. PhePhe NT have been integrated in devices for electronic and biosensing applications [11–13]. These nanostructures display unique and extraordinary mechanical properties: they are very stiff with a high averaged point stiffness and Young's modulus of 160 N/m and 19-27 GPa respectively, placing them among the stiffest biological materials known [14]. Due to the chirality of L-phenylalanine amino-acid, PhePhe NT are noncentrosymmetric structures which crystalize in $P6_{1,5}$ space group [8]. An effective nonlinear optical coefficient similar ($d_{eff} = 12\ pmV^{-1}$) has been reported for PhePhe NT [15]. However, for an all-organic crystalline material, the PhePhe nonlinearity is one order of magnitude smaller than those displayed by some state-of-the-art organic crystals like 2-methyl-4-nitroaniline (MNA) [16].

An analogue of PhePhe dipeptide structural family is the amine-modified Boc-L-phenylalanyl-L-phenylalanine (hereafter Boc-PhePhe, Boc= tert-butoxycarbonyl) that forms various nanoscale structures such as nanospheres (NS) [17] and NT [18]. Directional intermolecular π-π interactions and hydrogen-bonding networks originate quantum confined (QC) structures (that is, nanocrystalline regions possessing strong QC properties) within PhePhe, Boc-PhePhe and Boc-*p*-nitro-L-phenylalanyl-*p*-nitro-L-phenylalanine (hereafter Boc-*p*NPhe*p*NPhe) self-assemblies with pronounced exciton effects [19–21]. This last one, Boc-*p*NPhe*p*NPhe is the first dipeptide reported as displaying dual self-assembling from 1,1,1,3,3,3-hexafluoro-2-propanol (HFP) and water solutions: it self-assembles into microtapes which are themselves formed from self-assembly of nanotubes [22].

All amino acids, with exception of glycine, naturally display a chiral molecular structure and crystallize therefore with no center of symmetry. The lack of a center of a symmetry allows properties such as piezoelectricity and optical second harmonic generation to be displayed by the crystalline compounds. Consequently, dipeptides formed from chiral L-phenylalanine amino acid or derivatives, are non-centrosymmetric bio-active systems for exploring those properties. The piezoelectric properties of self-assembled Boc-*p*NPhe*p*NPhe, Figure 1, when embedded into electrospun polymer fibers have been reported recently and it was found that both dipeptide hybrid systems show a strong piezoelectric response to an applied periodical deformation [22].

Although the molecular self-assembling of these diphenylalanine derivatives has been study in great extension, the solid-state crystalline structure is known only for Boc-PhePhe dieptide. In this work we report the crystal structure of Boc-*p*NPhe*p*NPhe determined by single crystal X-ray diffraction at 100 K. Also, because the crystal space group is acentric, the optical second harmonic generation (SHG) property of Boc-*p*NPhe*p*NPhe microtapes is also reported.

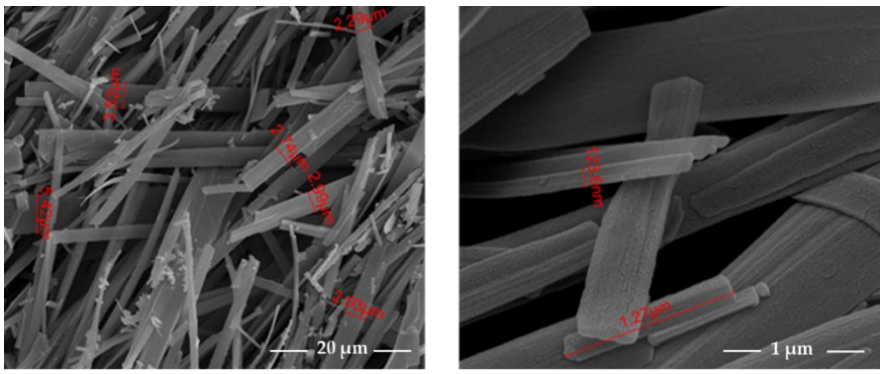


**Figure 1.** SEM images of Boc-*p*-nitro-L-phenylalanyl-*p*-nitro-L-phenylalanine (Boc= tert-butoxycarbonyl) dipeptide crystals at 5,000x and 100,000x magnifications. (Reproduced with permission from reference 22).

## 2. Experimental Section

### *2.1. Materials and Synthesis*

*p*-Nitro-L-phenylalanine (*p*NPhe), 1-hydroxybenzotriazole (HOBt), N,N-dicyclohexylcarbodiimide (DCC), thionyl chloride, and di-tert-butylpyrocarbonate ($Boc_2O$) were

 doi:10.20944/preprints202411.1376.v1



purchased from Sigma-Aldrich or Alfa Aesar and used without further purification. All solvents were purchased from Sigma-Aldrich and used as received.

The synthesis began by protecting the acid terminal of pNPhe through reaction with thionyl chloride in methanol, yielding the corresponding methyl ester of the amino acid. Then, the amino terminal was protected by reaction with di-tert-butylpyrocarbonate, resulting in the N-Boc-protected amino acid. The dipeptide was obtained by liquid-phase synthesis, coupling the amino acid methyl ester with the N-Boc-protected amino acid, using DCC/HOBt as coupling agents.

Further details of the synthesis can be found in the previously published article [22].

### *2.2. Differential Scanning Calorimetry (DSC) and Thermogravimetric Analysis (TGA) SI*

Differential scanning calorimetry (DSC) (**SI1**) analysis was performed in a Netzsch 200 Maya (Netzsch, Selb, Germany) under nitrogen flow (50 mL/min). The sample was placed in an aluminium pan. Two heating and one cooling ramp were run at: 2 °K/min, from: -30 °C to 200 °C . Thermogravimetric analysis (TGA) (**SI2**) was performed using a TA Q500 thermogravimetric analyzer (TA Instruments, New Castle, DE, USA). The sample was placed in a platinum crucible and heated from 30 °C to 700 °C at a heating rate of 10 °C/min under a nitrogen flow (60 mL/min).

### *2.3. Single-Crystal X-ray Diffraction*

Single-crystal X-ray diffraction data (ϕ scans and ω scans with κ and θ offsets) were collected on a Bruker D8 Venture diffractometer configured in κ-geometry, equipped with a Photon II CPAD detector and an IμS 3.0 Incoatec microfocus source Cu K$\alpha$ ($\lambda$ = 1.54178 Å). A suitable crystal of the compound was selected and mounted on a Kapton fiber using a MiTeGen MicroMount with immersion oil. Data collection was performed at 100 K with an Oxford Cryostream cryostat (800 series Cryostream Plus) attached to the diffractometer. The APEX 4 software [23] was used for unit cell determination and data collection. Data reduction and global cell refinement were carried out with the Bruker SAINT+ software package [24], and an absorption correction was applied using a multi-scan method via SADABS [25]. The structure was solved through intrinsic phasing using ShelXT (Sheldrick, 2015b) within the Olex2 interface [26] to the SHELX suite, allowing the location of most non-hydrogen atoms. Remaining non-hydrogen atoms were identified from Fourier difference maps calculated through successive full-matrix least-squares refinement cycles on $F^2$ using ShelXL[27] and refined with anisotropic displacement parameters. Hydrogen atoms were placed geometrically and refined using the riding model. Artwork representations were prepared using MERCURY [28] and PLATON [29]. The crystallographic data reported here are available under accession number CCDC: 2391827 and can be obtained free of charge from the Cambridge Crystallographic Data Centre at https://www.ccdc.cam.ac.uk/structures. Tables and the CIF file were generated using FinalCif [30].

### *2.4. Second Harmonic Generation*

The second harmonic signal were obtained using a mode-locked Ti:Sapphire oscillator (Coherent Mira) with a nominal pulse duration of 100 fs running at a repetition rate of 76 MHz. Details of the experimental set-up have been described previously [31]. Briefly, a combination half-wave plate and polarizer was employed to control the incident power onto the samples. The incident beam was focused using a x10 microscope objective with a numerical aperture of 0.25 and an effective focal length of 16.5 mm, producing a spot of approximately 40 μm ($1/e^2$) diameter in the focal plane. The resulting second harmonic signal in transmission was collected using a second objective (x20 with a numerical aperture of 0.4), filtered by a dichroic mirror, then passed through a combination zero-order half-wave plate and fixed calcite polarizer, before being filtered using a low-pass cut-off filter with a transition wavelength of 650 nm and focused into a multimode fibre bundle. At the output of the fibre bundle, a 0.3 m imaging spectrometer (Shamrock 303i form Andor) isolated the second harmonic signal around 400 nm. A cooled CCD camera (Newton 920 from Andor) was employed to capture the signal which was integrated over the roughly Gaussian profile of the second harmonic spectrum.

 doi:10.20944/preprints202411.1376.v1



Before the focusing objective and after the collimating objective zero-order half-wave-plates at 800 nm and 400 nm respectively were used to control the incident and detected linear polarization states. Two different polarization curves are presented "q-p" and "q-s". The "q-p" curve corresponds to the case when the transmitted polarization is that which gives rise to the maximum second harmonic signal. The half-wave-plate before focusing objective is then rotated to varying the fundamental polarization of the incident light. For the "q-s" the transmitted linear polarization state was set orthogonal to the "q-p" orientation and again the incident linear polarization was varied using the half-wave plate.

## 3. Results and Discussion

### *3.1. Crystal Structure of Boc-pNPhepNPhe*

Boc-*p*NPhe*p*NPhe crystallizes in the monoclinic crystal system, specifically in the non-centrosymmetric space group P2 (Table 1). The unit cell parameters are a = 12.4892(3) Å, b = 5.11310(10) Å, c = 18.7509(4) Å, and β = 90.4730(10)º. The asymmetric unit contains a single molecule, as illustrated in Figure 2. Despite possessing bonds that allow significant conformational flexibility, the molecular conformation of Boc-*p*NPhe*p*NPhe in the crystalline state is stabilized by a network of intramolecular hydrogen bonds, depicted as green dashed lines in Figure 2. Furthermore, the near-zero value of the Flack parameter confirms that the absolute configuration was properly determined.

Notably, the intramolecular hydrogen bonds C8–H8···O2 with a distance of 2.773(3) Å and C10–H10···O3 at 2.806(3) Å are among the strongest in Boc-*p*NPhe*p*NPhe, playing a critical role in defining its molecular conformation. Despite these constraints, a geometry check performed using the Mogul routine [32] from the Cambridge Structural Database did not reveal any geometrical parameters significantly deviating from average values.

**Table 1.** Crystal data and structure refinement for Boc-*p*NPhe*p*NPhe.

| | |
|---|---|
| CCDC number | 2391827 |
| Empirical formula | $C_{23}H_{26}N_4O_9$ |
| Formula weight | 502.48 |
| Temperature [K] | 100.00 |
| Crystal system | monoclinic |
| Space group (number) | *P*2 (3) |
| *a* [Å] | 12.4892(3) |
| *b* [Å] | 5.11310(10) |
| *c* [Å] | 18.7509(4) |
| β [°] | 90.4730(10) |
| Volume [Å$^3$] | 1197.36(5) |
| *Z* | 2 |
| $\rho_{calc}$ [gcm$^{-3}$] | 1.394 |
| $\mu$ [mm$^{-1}$] | 0.921 |
| *F*(000) | 528 |
| Crystal size [mm$^3$] | 0.026×0.043×0.443 |
| Crystal colour | clear light colourless |
| Crystal shape | needle |
| Radiation | Cu$K_\alpha$ ($\lambda$=1.54178 Å) |
| 2θ range [°] | 7.08 to 144.49 (0.81 Å) |

 doi:10.20944/preprints202411.1376.v1



| | |
|---|---|
| Reflections collected | 52422 |
| Independent reflections | 4670, $R_{int}$ = 0.0772, $R_{sigma}$ = 0.0315 |
| Data / Restraints / Parameters | 4670 / 1 / 328 |
| Goodness-of-fit on $F^2$ | 1.018 |
| Final $R$ indexes [$I \geq 2\sigma(I)$] | $R_1$ = 0.0357 w$R_2$ = 0.0870 |
| Final $R$ indexes [all data] | $R_1$ = 0.0427, w$R_2$ = 0.0927 |
| Largest peak/hole [eÅ$^{-3}$] | 0.25/−0.24 |
| Flack X parameter | -0.06(9) |

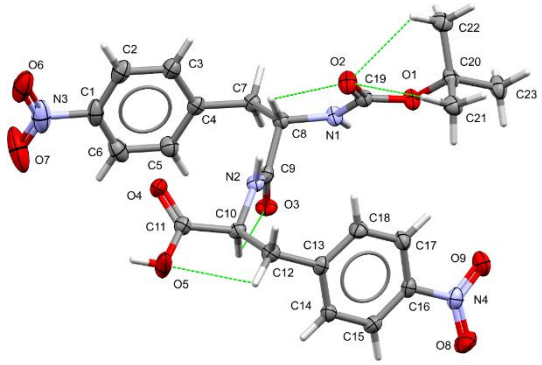


**Figure 2.** Boc-*p*NPhe*p*NPhe dipeptide asymmetric cell. Green dashed lines represent intramolecular hydrogen bonds.

The predominant feature in the crystal packing of Boc-pNPhepNPhe is the formation of a dimer through a homosynthon interaction between the carboxylic groups, creating an $\boldsymbol{R_2^2(8)}$ motif centered around the 2-fold axis, as observed in the ac-projection of the crystal structure shown in Figure 3a). This dimer is stabilized by a strong O5–H5···O4 hydrogen bond, with its parameters listed in Table 2. The relative orientation of the molecules within the dimer is further defined by a weak hydrogen bond, C14–H14A···O7, which together with the strong hydrogen bond determines the final geometry of the dimer.

Preprints.org (www.preprints.org) | NOT PEER-REVIEWED | Posted: 19 November 2024 doi:10.20944/preprints202411.1376.v1



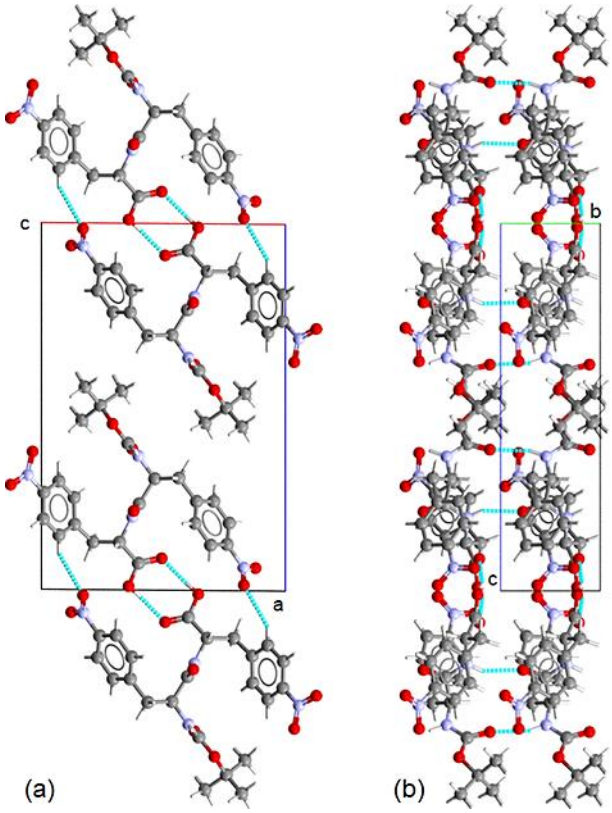


**Figure 3.** Projections of the crystalline structure of the Boc-*p*NPhe*p*NPhe: (a) ac-plane and (b) bc-plane.

**Table 2.** Intermolecular hydrogen bond parameters for Boc-pNPhepNPhe (Distances in Å and Angles in °).

| D–H···A | d(H···A) | d(D···A) | <(DHA) |
|---|---|---|---|
| O5–H5···O4#1 | 1.83 | 2.625(3) | 158 |
| N1–H1···O2#2 | 2.09 | 2.935(3) | 162 |
| N2–H2···O3#3 | 2.09 | 2.892(3) | 151 |
| C2–H2A···O8#4 | 2.42 | 3.089(4) | 129 |
| C5–H5A···O4#2 | 2.53 | 3.286(4) | 136 |
| C14–H14A···O7#1 | 2.49 | 3.350(4) | 151 |

Symmetry transformations used to generate equivalent atoms: #1: 1-x,y,-z; #2: x,-1+y,z; #3: x,1+y,z; #4: 1+x,1+y,z

The stacking of the strongly bonded dimers along the b-axis is facilitated by the trans configuration of the two amide moieties. This arrangement allows the formation of infinite chains through strong N1–H1···O2 and N2–H2···O3 hydrogen bonds, as illustrated in the bc-projection of the structure depicted in Figure 3b). These chains are further stabilized by two π–π interactions between rings of the same type (4.7127(15) Å), as well as by the weak hydrogen bond C5–H5A···O4.

Hydrogen bonds do not play a key role in the packing of the amide chains, as only a hydrogen bond (C2–H2A···O8) links laterally dimers from consecutive layers. To gain a more comprehensive understanding of the crystal packing, we performed Hirshfeld surface (HS) analysis mapped with the shape index and generated two-dimensional fingerprint (2DF) plots using the CrystalExplorer software [33]. Mapping the HS with the shape index allows for the identification and visualization of

 doi:10.20944/preprints202411.1376.v1



specific intermolecular interactions, such as π–π and X–Y···π interactions, by highlighting complementary regions on the molecular surface. The 2DF plots condense this information into graphical representations that map the frequency and nature of contact points between molecules. These analytical tools are invaluable for comparing and clustering structures, identifying structural similarities, and extracting relevant information about intermolecular interactions [34–36].

The HS and 2DF plots are presented in Figure 4, where the regions above the aromatic rings are labeled ❶ and ❷. Notably, the characteristic red and blue triangles forming a 'bow-tie' pattern over ring ❶ highlight the π–π interactions associated with the dimer stacking of the amide chains (Figure 4a). Above ring ❷, the HS mapping is less defined, displaying two diffuse 'bow-tie' patterns related to two π–π bonds: one associated with the stacking and a stronger interaction (4.7127(15) Å) between rings of different types, which contributes to the packing of the chains. In this region, a red depression indicates the N4–O8···π interaction (3.449(3) Å), is also contributing to the alignment of the parallel chains. This latter interaction is observable in the 2DF plot through the frequency of the C–O distances, which exhibit the wing-like pattern commonly associated with C–H···π interactions (Figure 4b). Finally, it is noteworthy that the 2DF plot is dominated by two strong spikes corresponding to O–H distances, highlighting the key role of the carboxylic–carboxylic and amide–amide interactions in forming and stacking the Boc-*p*NPhe*p*NPhe dimers.

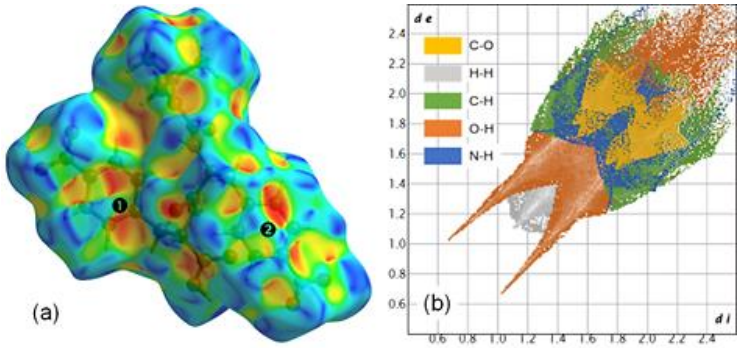


**Figure 4.** (a) Hirshfeld surface of Boc-*p*NPhe*p*NPhe mapped with the shape index, with labels ❶ and ❷ highlighting regions over the aromatic rings. (b) Corresponding 2D fingerprint plot; the colour coding of distance pair frequencies includes reciprocal contacts.

### *3.4. Optical Second Harmonic Generation*

Second harmonic generation (SHG) is a nonlinear optical process, where a fundamental wave of frequency ω, incident on an acentric crystalline medium, generates another optical wave of frequency 2ω, due to the nonlinear polarization of the medium. Biological materials such as proteins, collagen and viruses, are known to exhibit SHG phenomena due to their non-centrosymmetric structures [37]. This property is described by a 3rd rank tensor, where the tensor elements are determined by the crystal point group symmetry [38]. Although SHG has been studied in great extension in several organic crystals, very few studies have been reported on dipeptide crystals.

In this work we measured SHG on Boc-*p*NPhe*p*NPhe crystal microtapes, which belong to crystallographic point group 2, the crystals are therefore biaxial. Assuming Kleinman symmetry, the second harmonic light polarization for this point group takes the general form:

$$\begin{bmatrix} P_1^{2\omega} \\ P_2^{2\omega} \\ P_3^{2\omega} \end{bmatrix} = \begin{bmatrix} 0 & 0 & 0 & d_{14} & 0 & d_{21} \\ d_{21} & d_{22} & d_{23} & 0 & d_{14} & 0 \\ 0 & 0 & 0 & d_{23} & 0 & d_{14} \end{bmatrix} \begin{bmatrix} E_1^{\omega}E_1^{\omega} \\ E_2^{\omega}E_2^{\omega} \\ E_3^{\omega}E_3^{\omega} \\ 2E_2^{\omega}E_3^{\omega} \\ 2E_1^{\omega}E_3^{\omega} \\ 2E_1^{\omega}E_2^{\omega} \end{bmatrix}$$

Preprints.org (www.preprints.org) | NOT PEER-REVIEWED | Posted: 19 November 2024 doi:10.20944/preprints202411.1376.v1



Here $E_1, E_2$ and $E_3$ are the electric fields associated, with the fundamental optical wave; $P_1^{2\omega}, P_2^{2\omega}, P_3^{2\omega}$ are the nonlinear polarizations generated inside the medium and $d_{ij}$ i,j=1,2,3 are the non-linear optical crystal coefficients. In Figure 5. It is plotted the second harmonic polarimetry curves for a Boc-*p*NPhe*p*NPhe crystal. For the q-p cure the analyser was oriented along the direction of the strongest second harmonic response, while for the q-s curve the analyser was aligned perpendicular to that direction. In both curves the angle q represents the orientation of the incident linear polarization relative to the analyser direction along which the strongest second harmonic signal was observed. The incident fundamental optical wave vector was perpendicular to the crystallographic *b* axis, which is assingned to the dielectric y axis. Due to the difficulty in growing sizeable crystal for the determination of the *x* and *z* dielectric axis, it was not possible to determine their location and orientation relatively to the crystallographic *a* and *b* axis. As such, in this work we will only measure an effective coefficient $d_{eff}$, from the crystal response.

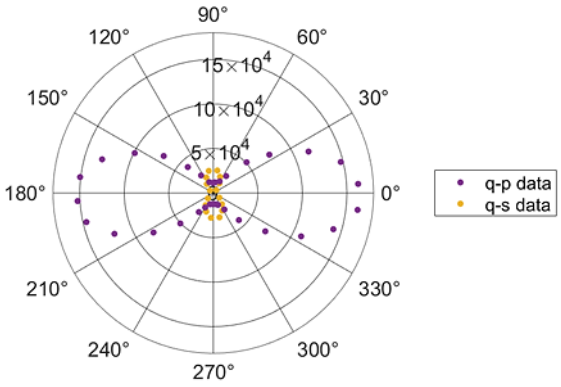


**Figure 5.** The second harmonic signal generated by Boc-*p*NPhe*p*NPhe crystal microtapes as a function of the orientation of the fundamental beam's polarization orientation relative to the transmission axis of the analyzer.

The Boc *p*NPhe*p*NPhe micro tapes q-p curve displays very nearly a pure $\boldsymbol{cos^4(\theta)}$ dependence, which occurs when the second harmonic response of a crystalline material is dominated by a single tensor element of the second order nonlinear coefficient, as shown in Figure 5. However, the q-p curve does not go to zero at 90 and 270 degrees, which results from the fact that for a monoclinic unit cell, the dielectric axis does not coincide with the crystallographic axis. We obtain a good fit to the experimental data, by assuming that there is a small contribution with an orthogonal orientation added in quadrature to the dominate term. Figure 6. shows the fit to the q-p curve by a function of the form $[A\ cos^4(\theta) + BA\ sin^4(\theta)]$ with A = (1.62±0.01) x$10^5$ counts and B = (1.3±0.1) x$10^4$ counts.

Preprints.org (www.preprints.org) | NOT PEER-REVIEWED | Posted: 19 November 2024 doi:10.20944/preprints202411.1376.v1



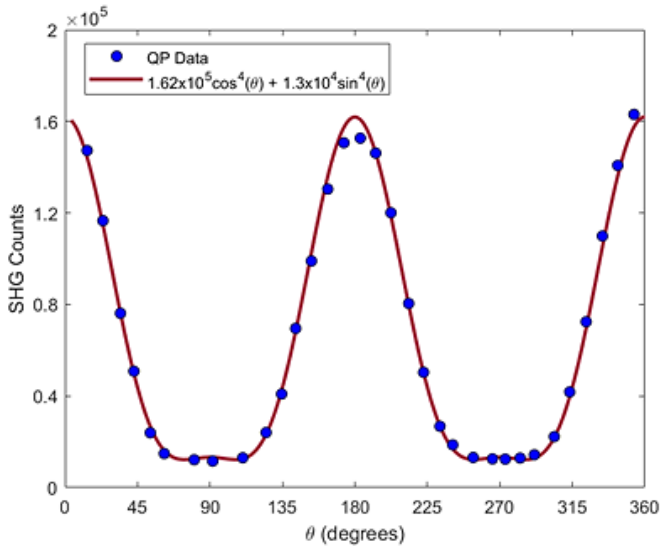


**Figure 6.** The second harmonic response as the crystal was translated in 10 μm steps along the propagation direction of the fundamental beam. Also shown is a theoretical fit assuming Gaussian spatial and temporal profiles for the two beams.

To estimate the effective second order nonlinear susceptibility, we have used a 2 mm thick BBO (Barium Beta Borate, from EKSMA, crystal) cut for phase matching at an incident fundamental wavelength of 800 nm, to calibrate the detection efficiency of our experimental set-up. For the strong focusing condition created by the x10 microscope objective, the effective length of the BBO crystal that generates second harmonic light is limited to approximately 30 μm by the spatial walk-off angle of BBO which is 68 mradians for the second harmonic light. Details of the procedure used have been previously published [39]. The relevant parameters and final results are summarized in Table 3.

**Table 3.** Second harmonic generation parameters for Boc-*p*NPhe*p*NPhe crystal microtapes.

| **Single Crystal** | **Fundamental wave power (mW)** | **Signal integration time (ms)** | **Effective thickness (μm)** | **Second harmonic signal (counts)** | $d_{eff}$ **(pm/V)** |
|---|---|---|---|---|---|
| BBO | 0.5 | 2.5 | 30 | $2.4\times10^{6}$ | 2.0 |
| Boc-*p*NPhe*p*NPhe | 5 | 250 | 0.5 | $1.6\times10^{5}$ | 0.52 |

It should be that the second harmonic signals acquired from Boc-*p*NPhe*p*NPhe micro tapes was under normal incidence, no attempt was made to optimized the angle of the fundamental beams wave-vector and therefore the phase-match condition was not achieved. As such the value in Table 3 for Boc-*p*NPhe*p*NPhe, represents a lower bound on the estimate of the respective effective coefficient value. Also, as we are determining a non-linear effective coefficient value it means that some coefficients may have magnitudes one or two order of magnitude bigger.

## 4. Conclusions

Boc-*p*NPhe*p*NPhe is a dipeptide which self-assembles into microtapes and crystallizes in the non-centrosymmetric space group P2 with a single molecule in the asymmetric unit. The molecular conformation of Boc-*p*NPhe*p*NPhe in the crystalline structure is stabilized by a network of intramolecular hydrogen bonds althought possessing bonds that allow significant conformational flexibility. In particular, C8–H8···O2 with a distance of 2.773(3) Å and C10–H10···O3 at 2.806(3) Å intramolecular hydrogen bonds play a fundamental role in Boc-pNPhepNPhe molecular conformation. The key feacture in the crysral unit cell packing is the formation of a dimer through a homosynthon interaction between the carboxylic groups, centered on the 2-fold axis. Moreover,

through strong N1–H1···O2 and N2–H2···O3 hydrogen bonds infinite chains along the b-axis are formed as a result of a stack of the strong bonded dimers along that 2.fold axis.

Hirshfeld surface and two-dimensional fingerprint plots of Boc-*p*NPhe*p*NPhe show in regions above the aromatic rings a 'bow-tie' pattern highlighting the π–π interactions associated with the dimer stacking of the amide chains. The key role of carboxylic–carboxylic and amide–amide interactions in the formation and stacking of the Boc-pNPhepNPhe dimers are evidenced by the two strong spikes.

Thermal measurements show that the crystalline compound is stable until near 190ºC.

The crystal point group allows nonlinear optical effects to exist. Second harmonic measurements and calculations performed, revealed an effective second order nonlinear susceptibility coefficient $d_{eff}$ higher than 0.52 pm/V, measured against a state-of-the-art phase matched BBO (Barium Beta Borate) crystal. This result indicates that Boc-*p*NPhe*p*NPhe dipeptide is a promising nonlinear optical dipeptide, envisioning that some nonlinear optical coefficients may have magnitudes one or two orders of magnitude higher than the effective coefficient measured.

**Supplementary Materials:** The following supporting information can be downloaded at the website of this paper posted on Preprints.org, S1: TGA and DSC Analysis; S2: Crystal data; Figure S1: DSC and TGA spectra; Table S2.1: Atomic coordinates; Table S2.2: Anisotropic displacement parameters; Table S2.3: Bond lengths and angles; Table S2.4: Torsion angles.

**Author Contributions:** Rosa M. F. Baptista and Etelvina de Matos Gomes conceived and coordinated all the work, analysed the results, wrote and edited the manuscript. Michael S. Belsley supervised the experimental non-linear optical work and wrote and edit the manuscript document. M. Cidália R. Castro and Ana. V. Machado carried out the DSC and TGA analyses. Alejandro P. Ayala performed the single crystal X-ray structure determination, Hirshfeld analysis and wrote and edit the manuscript. All authors discussed and commented on the manuscript.

**Funding:** This research was funded by Fundação para a Ciência e Tecnologia through FEDER (European Fund for Regional Development)-COMPETE-QREN-EU (ref. UID/FIS/04650/2013 and UID/FIS/04650/2019).

**Institutional Review Board Statement:** This study did not involve humans or animals.

**Informed Consent Statement:** This study did not involve humans or animals.

**Acknowledgements:** Rosa M. F. Baptista acknowledges for her contract DL57/2016, with reference DL 57/2016/CP1377/CT0064 (DOI:10.54499/DL57/2016/CP1377/CT0064). The authors acknowledge Cesar Bernardo for collecting the nonlinear optical data.

**Conflicts of Interest:** The authors declare no conflict of interest.

## References

1. Liu, H.; Xu, J.; Li, Y.; Li, Y. Aggregate Nanostructures of Organic Molecular Materials. *Accounts Chem. Res.* **2010**, *43*, 1496-1508, doi:10.1021/ar100084y.
2. Berger, O.; Adler-Abramovich, L.; Levy-Sakin, M.; Grunwald, A.; Liebes-Peer, Y.; Bachar, M.; Buzhansky, L.; Mossou, E.; Forsyth, V.T.; Schwartz, T.; et al. Light-emitting self-assembled peptide nucleic acids exhibit both stacking interactions and Watson–Crick base pairing. *Nature Nanotech.* **2015**, *10*, 353-360, doi:10.1038/nnano.2015.27.
3. Apter, B.; Lapshina, N.; Handelman, A.; Fainberg, B.D.; Rosenman, G. Peptide Nanophotonics: From Optical Waveguiding to Precise Medicine and Multifunctional Biochips. *Small* **2018**, *14*, 1801147, doi:10.1002/smll.201801147.
4. Ariga, K.; Nishikawa, M.; Mori, T.; Takeya, J.; Shrestha, L.K.; Hill, J.P. Self-assembly as a key player for materials nanoarchitectonics. *Sci. technol. adv. material* **2019**, *20*, 51-95, doi:10.1080/14686996.2018.1553108.
5. Ghadiri, M.R. Self-Assembled Nanoscale Tubular Ensembles. *Adv. Mater.* **1995**, *7*, 675-677, doi:DOI 10.1002/adma.19950070718.
6. Gilead, S.; Gazit, E. Self-organization of short peptide fragments: From amyloid fibrils to nanoscale supramolecular assemblies. *Supramol. Chem.* **2005**, *17*, 87-92, doi:10.1080/10610270412331328943.
7. Gorbitz, C. Hydrophobic dipeptides: the final piece in the puzzle. *Acta Crystallogr. B* **2018**, *74*, 311-318, doi:doi:10.1107/S2052520618007151.
8. Gorbitz, C.H. Nanotube formation by hydrophobic dipeptides. *Chem.-Eur. J.* **2001**, *7*, 5153-5159, doi:Doi 10.1002/1521-3765(20011203)7:23<5153::Aid-Chem5153>3.0.Co;2-N.

9. Kim, J.; Han, T.H.; Kim, Y.I.; Park, J.S.; Choi, J.; Churchill, D.C.; Kim, S.O.; Ihee, H. Role of Water in Directing Diphenylalanine Assembly into Nanotubes and Nanowires. *Adv. Mater.* **2010**, *22*, 583-+, doi:10.1002/adma.200901973.
10. Li, Q.; Jia, Y.; Dai, L.; Yang, Y.; Li, J. Controlled Rod Nanostructured Assembly of Diphenylalanine and Their Optical Waveguide Properties. *ACS Nano* **2015**, *9*, 2689-2695, doi:10.1021/acsnano.5b00623.
11. Adler-Abramovich, L.; Gazit, E. The physical properties of supramolecular peptide assemblies: from building block association to technological applications. *Chem. Soc. Rev.* **2014**, *43*, 6881-6893, doi:10.1039/C4CS00164H.
12. Allafchian, A.R.; Moini, E.; Mirahmadi-Zare, S.Z. Flower-Like Self-Assembly of Diphenylalanine for Electrochemical Human Growth Hormone Biosensor. *IEEE Sensors J.* **2018**, *18*, 8979-8985, doi:10.1109/JSEN.2018.2869071.
13. Cipriano, T.; Knotts, G.; Laudari, A.; Bianchi, R.C.; Alves, W.A.; Guha, S. Bioinspired Peptide Nanostructures for Organic Field-Effect Transistors. *ACS Appl. Mater. Inter.* **2014**, *6*, 21408-21415, doi:10.1021/am5064124.
14. Kol, N.; Adler-Abramovich, L.; Barlam, D.; Shneck, R.Z.; Gazit, E.; Rousso, I. Self-assembled peptide nanotubes are uniquely rigid bioinspired supramolecular structures. *Nano Lett.* **2005**, *5*, 1343-1346, doi:10.1021/nl0505896.
15. Handelman, A.; Lavrov, S.; Kudryavtsev, A.; Khatchatouriants, A.; Rosenberg, Y.; Mishina, E.; Rosenman, G. Nonlinear Optical Bioinspired Peptide Nanostructures. *Adv. Opt. Mater.* **2013**, *1*, 875-884, doi:https://doi.org/10.1002/adom.201300282.
16. Isakov, D.; de Matos Gomes, E.; Belsley, M.S.; Almeida, B.; Cerca, N. Strong enhancement of second harmonic generation in 2-methyl-4-nitroaniline nanofibers. *Nanoscale* **2012**, *4*, 4978-4982, doi:10.1039/C2NR30771E.
17. Adler-Abramovich, L.; Gazit, E. Controlled patterning of peptide nanotubes and nanospheres using inkjet printing technology. *J. Pept. Sci.* **2008**, *14*, 217-223, doi:10.1002/psc.963.
18. Adler-Abramovich, L.; Kol, N.; Yanai, I.; Barlam, D.; Shneck, R.Z.; Gazit, E.; Rousso, I. Self-Assembled Organic Nanostructures with Metallic-Like Stiffness. *Angew. Chem. Int. Ed.* **2010**, *49*, 9939-9942, doi:10.1002/anie.201002037.
19. Tao, K.; Fan, Z.; Sun, L.; Makam, P.; Tian, Z.; Ruegsegger, M.; Shaham-Niv, S.; Hansford, D.; Aizen, R.; Pan, Z.; et al. Quantum confined peptide assemblies with tunable visible to near-infrared spectral range. *Nat. Commun.* **2018**, *9*, 3217, doi:10.1038/s41467-018-05568-9.
20. Amdursky, N.; Molotskii, M.; Aronov, D.; Adler-Abramovich, L.; Gazit, E.; Rosenman, G. Blue Luminescence Based on Quantum Confinement at Peptide Nanotubes. *Nano Lett.* **2009**, *9*, 3111-3115, doi:10.1021/nl9008265.
21. Baptista, R.M.F.; de Matos Gomes, E.; Raposo, M.M.M.; Costa, S.P.G.; Lopes, P.E.; Almeida, B.; Belsley, M.S. Self-assembly of dipeptide Boc-diphenylalanine nanotubes inside electrospun polymeric fibers with strong piezoelectric response. *Nanoscale Adv.* **2019**, *1*, 4339-4346, doi:10.1039/C9NA00464E.
22. Baptista, R.M.F.; Lopes, P.E.; Rodrigues, A.R.O.; Cerca, N.; Belsley, M.S.; de Matos Gomes, E. Self-assembly of Boc-p-nitro-l-phenylalanyl-p-nitro-l-phenylalanine and Boc-l-phenylalanyl-l-tyrosine in solution and into piezoelectric electrospun fibers. *Materials Adv.* **2022**, *3*, 2934-2944, doi:10.1039/D1MA01022K.
23. Bruker, A.X.S.I. *APEX4 suite*, Madison, Wisconsin, USA, 2021.
24. Bruker, A.X.S.I. *SAINT+ Data Reduction Software*, Madison, Wisconsin, USA, 2019.
25. Krause, L.; Herbst-Irmer, R.; Sheldrick, G.M.; Stalke, D. Comparison of silver and molybdenum microfocus X-ray sources for single-crystal structure determination. *J. Appl. Crystallogr.* **2015**, *48*, 3-10, doi:10.1107/S1600576714022985.
26. Dolomanov, O.V.; Bourhis, L.J.; Gildea, R.J.; Howard, J.A.K.; Puschmann, H. OLEX2: a complete structure solution, refinement and analysis program. *J. Appl. Crystallogr.* **2009**, *42*, 339-341, doi:10.1107/s0021889808042726.
27. Sheldrick, G.M. Crystal structure refinement with SHELXL. *Acta Crystallogr.. C Struct. Chem.* **2015**, *71*, 3-8, doi:10.1107/S2053229614024218.
28. Macrae, C.F.; Sovago, I.; Cottrell, S.J.; Galek, P.T.A.; McCabe, P.; Pidcock, E.; Platings, M.; Shields, G.P.; Stevens, J.S.; Towler, M.; et al. Mercury 4.0: from visualization to analysis, design and prediction. *J. Appl. Crystallogr.* **2020**, *53*, 226-235, doi:10.1107/S1600576719014092.
29. Spek, A.L. Structure validation in chemical crystallography. *Acta Crystallogr. D Biol. Crystallogr.* **2009**, *65*, 148-155, doi:10.1107/S090744490804362X.
30. Kratzert, D. *FinalCif*, 2023.
31. Baptista, R.M.F.; Gomes, C.S.B.; Silva, B.; Oliveira, J.; Almeida, B.; Castro, C.; Rodrigues, P.V.; Machado, A.; Freitas, R.B.; Rodrigues, M.J.L.F.; et al. A Polymorph of Dipeptide Halide Glycyl-L-Alanine Hydroiodide Monohydrate: Crystal Structure, Optical Second Harmonic Generation, Piezoelectricity and Pyroelectricity. *Materials* **2023**, *16*, doi:10.3390/ma16103690.

32. Bruno, I.J.; Cole, J.C.; Kessler, M.; Luo, J.; Motherwell, W.D.; Purkis, L.H.; Smith, B.R.; Taylor, R.; Cooper, R.I.; Harris, S.E.; et al. Retrieval of crystallographically-derived molecular geometry information. *J. Chem. Inf. Comput. Sci.* **2004**, *44*, 2133-2144, doi:10.1021/ci049780b.
33. Spackman, P.R.; Turner, M.J.; McKinnon, J.J.; Wolff, S.K.; Grimwood, D.J.; Jayatilaka, D.; Spackman, M.A. CrystalExplorer: a program for Hirshfeld surface analysis, visualization and quantitative analysis of molecular crystals. *J. Appl. Crystallogr.* **2021**, *54*, 1006-1011, doi:10.1107/S1600576721002910.
34. Fonseca, J.d.C.; Tenorio Clavijo, J.C.; Alvarez, N.; Ellena, J.; Ayala, A.P. Novel Solid Solution of the Antiretroviral Drugs Lamivudine and Emtricitabine. *Cryst. Growth Des.* **2018**, *18*, 3441-3448, doi:10.1021/acs.cgd.8b00164.
35. Santiago de Oliveira, Y.; Saraiva Costa, W.; Ferreira Borges, P.; Silmara Alves de Santana, M.; Ayala, A.P. The design of novel metronidazole benzoate structures: exploring stoichiometric diversity. *Acta Crystallogr. C Struct. Chem.* **2019**, *75*, 483-495, doi:10.1107/S2053229619003838.
36. Spackman, M.A.; Jayatilaka, D. Hirshfeld surface analysis. *Cryst. Eng. Comm.* **2009**, *11*, 19-32, doi:10.1039/b818330a.
37. Delfino, M. A comprehensive optical second harmonic generation study of the non-centrosymmetric character of biological structures. *J. Biol. Phys.* **1978**, *6*, 105-117, doi:10.1007/BF02328933.
38. Nye, J.F. *Physical properties of crystals : their representation by tensors and matrices*, Repr. paperback ed. ed.; Oxford : Clarendon press: 2004.
39. Bernardo, C.R.; Baptista, R.M.F.; de Matos Gomes, E.; Lopes, P.E.; Raposo, M.M.M.; Costa, S.P.G.; Belsley, M.S. Anisotropic PCL nanofibers embedded with nonlinear nanocrystals as strong generators of polarized second harmonic light and piezoelectric currents. *Nanoscale Adv.* **2020**, *2*, 1206-1213, doi:10.1039/C9NA00687G.